Correlated atomic motions in the negative thermal expansion material ZrW$_2$O$_8$: A local structure study

D. Cao,[1] F. Bridges,[1] G. R. Kowach,[2] and A. P. Ramirez[3]

[1]*Physics Department, University of California, Santa Cruz, California 95064, USA*
[2]*Agere Systems, 600 Mountain Avenue, Murray Hill, New Jersey 07974-0636, USA*
[3]*MS-K764, Los Alamos National Laboratory, Los Alamos, New Mexico 87545, USA*

Recent studies of zirconium tungstate, ZrW$_2$O$_8$, show an isotropic negative thermal expansion (NTE) over a wide temperature range. It has been proposed that the low-energy phonon vibrational modes, observed in both specific heat and phonon density-of-states measurements, are responsible for this unusual NTE. We have carried out x-ray-absorption fine-structure (XAFS) experiments at both the W L_{III} edge and Zr K edge to study the detailed local structure in ZrW$_2$O$_8$. Our XAFS results show a very small temperature dependence of the broadening parameter, σ, for the W-Zr atom pair and the W-O-Zr linkage; consequently, the displacements of the W, O, and Zr atoms must be correlated. The data show a much larger temperature dependence of σ for the nearest W$_1$-W$_2$ pair as well as for the nearest Zr-Zr pair. These combined results indicate that it is the correlated motion of a WO$_4$ tetrahedron and its three nearest ZrO$_6$ octahedra that leads to the NTE effect in this material instead of primarily transverse vibrations of the middle O atom in the W-O-Zr linkage. The data for both W-W and Zr-Zr atom pairs also indicate a hardening of the effective spring constant near 100 K, which is consistent with the shift of the lowest mode with T in the phonon density of states. A simple model is developed to explain the NTE in terms of the local structure results; it also provides a natural explanation for the lack of a soft-mode phase transition.

I. INTRODUCTION

The negative thermal expansion (NTE) in ZrW$_2$O$_8$ was discovered long ago by Martinek and Hummel[1] and has attracted considerable attention recently due to its isotropic nature over a wide range of temperature (from 10 to 1050 K).[2,3] NTE has been studied in several different systems,[4–6] but most of them only show a small and anisotropic NTE effect over a small temperature range. The unusual NTE features of ZrW$_2$O$_8$ make it potentially useful in developing composites with easy-to-control thermal properties.

The crystal structure of zirconium tungstate, ZrW$_2$O$_8$, is cubic with the space group $P2_13$ at temperatures from 0 to $\sim$430 K, while the space group changes to $Pa\bar{3}$ as the temperature passes $\sim$430 K, with an order-to-disorder phase transition due to the disordering of the WO$_4$ tetrahedra.[2,7] An interesting feature of the ZrW$_2$O$_8$ crystal structure is that it consists of ZrO$_6$ octahedra and WO$_4$ tetrahedra which are connected via the corner O atoms. An important exception is that one O atom on each WO$_4$ tetrahedron is not connected to another unit and is therefore considered to be unconstrained. This O is located on a WO$_4$ vertex oriented along one of the $\langle 111 \rangle$ directions. Figure 1 shows the details of this structure.

It was first suggested by Mary *et al.* that a large transverse vibration of the oxygen in the middle of the W-O-Zr linkage, which requires corresponding rotations of the polyhedra, is the primary origin of NTE in this material due to the unconstrained feature of the structure.[2] A similar idea was used to explain the isotropic NTE in ZrV$_2$O$_7$ as temperature increases above 373 K,[8] i.e., the transverse vibration of the central O atom in the middle of the O$_3$V-O-VO$_3$ group.

ZrV$_2$O$_7$ has a similar structure to ZrW$_2$O$_8$ consisting of ZrO$_6$ octahedra and VO$_4$ tetrahedra. Three corners of a VO$_4$ tetrahedron are shared with ZrO$_6$ octahedra, but the fourth corner of each VO$_4$ tetrahedron is shared with another VO$_4$ tetrahedron and is therefore more highly constrained.

The calculation of rigid unit modes (RUMs) in these two materials, carried out by Pryde *et al.*,[9] pointed out that
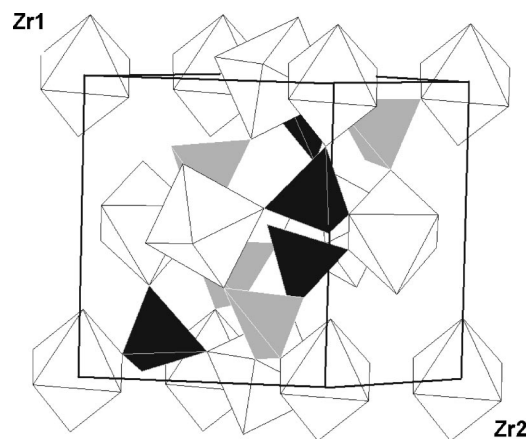

FIG. 1. The cubic unit-cell structure for ZrW$_2$O$_8$. The white polyhedra are the ZrO$_6$ octahedra; they occupy the corner and face-centered positions of the unit cell. The four gray and four black polyhedra are the W(1)O$_4$ and W(2)O$_4$ tetrahedra, respectively. Each tetrahedron shares its three corners with three other white octahedra while the last unshared corner is pointing along one of the four $\langle 111 \rangle$ axes. One of these $\langle 111 \rangle$ axes is between two isolated octahedra in this figure (the two octahedra marked Zr1 and Zr2); there are two tetrahedra on this $\langle 111 \rangle$ axis with their unshared corner pointing towards Zr$_1$.

RUMs are only possible in ZrW_2O_8. A comparison of the calculated vibration density of states for these two materials shows that many more low-frequency modes occur in ZrW_2O_8 than in ZrV_2O_7. Since ZrW_2O_8 exhibits NTE at very low temperatures, Pryde et al. suggested that the low-frequency rotations of rigid units contribute mainly to the NTE in this material, and the mechanism for NTE in ZrW_2O_8 and ZrV_2O_7 should be qualitatively different.[9]

The thermodynamics of this unusual system have been investigated by several groups in recent years.[3,10–14] In specific-heat data there is a very large contribution at low temperatures. To model these results, Ramirez and Kowach[10] used two low-energy Einstein modes (near 38 and 67 K) with a ratio of 1:3, respectively, in their density of states, plus smaller contributions from Debye modes with much higher Debye temperatures. Ernst et al.[11] measured the low-energy density of states using neutron scattering and found similar low-energy modes. In addition, using the modes below 8 meV they estimated the effective Grüneisen parameter and found it to be large and negative (-14). David et al.[3] also estimated the Grüneisen parameters but did so for each of the modes separately—in this analysis the two lowest modes both have negative Grüneisen parameters but the magnitude of the lower mode is roughly 20 times larger, while the higher-energy Debye modes have very small positive Grüneisen parameters. Recently Mittal et al.[14] investigated the change in phonon frequency with applied pressure and found that the low-frequency modes softened, hence the lowest modes have a negative Grüneisen parameter in agreement with the earlier work.[3,11] These studies clearly show that the low-energy optical modes play a dominant role in the NTE but detailed information about the atomic vibrations is not yet available, particularly information explaining which atoms are principally involved. In order to investigate the local structure of ZrW_2O_8 in detail, we have carried out x-ray-absorption fine-structure (XAFS) measurements as a function of temperature. From these data we obtain plots of σ^2 vs T from which an Einstein or Debye temperature can be extracted. This enables us to connect the local structure results to the modes found in the above studies. Some preliminary results have recently been published.[27]

The XAFS data show that the WO_4 tetrahedra are rigid from 5 up to ~320 K. The ZrO_6 octahedra are softer, although still quite stiff over the same temperature range, but they are not rigid. Surprisingly, the data analysis shows that the W-O-Zr linkage is also quite stiff, comparable to the ZrO_6 octahedra.

The data for the W(1)-W(2) and Zr-Zr atom pairs show much larger temperature dependencies, which are associated with low-frequency optical vibrational modes. These combined results indicate that the Zr, O, and W atomic motions are highly correlated; such correlations must be recognized in discussions of the low-energy vibrational modes. Based on these results, we propose a modified model for the eigenmodes that includes translations of the WO_4 as a rigid unit and leads to NTE in this material. This model also provides an explanation for both the unusually low energy of the optical modes and the lack of formation of a soft-mode displacive transition.
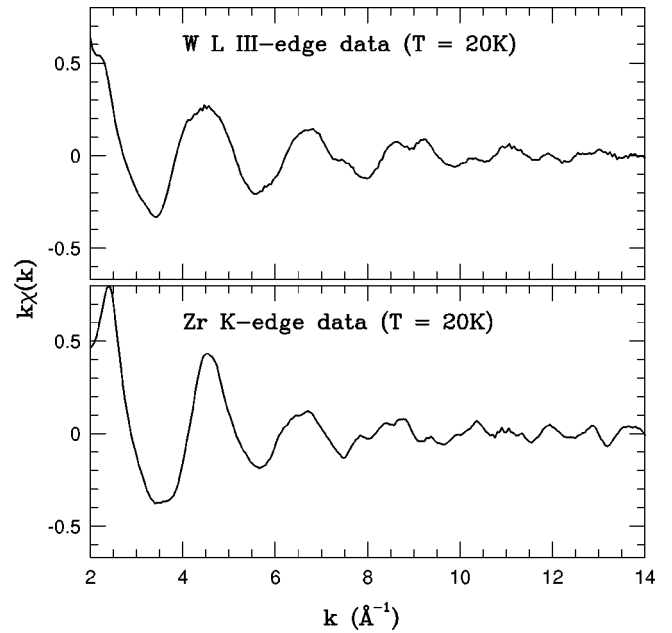

FIG. 2. $k\chi(k)$ vs k for both the W L_{III} and Zr K edges to show the quality of the XAFS data.

The experimental details and the sample information are given in Sec. II. Section III shows the XAFS data and analysis, while the discussion is presented in Sec. IV. The conclusions are summarized in Sec. V.

II. EXPERIMENT DETAILS

XAFS experiments were carried out at the Stanford synchrotron-radiation laboratory (SSRL) on beam line 10-2 with silicon $\langle 220 \rangle$ monochromator crystals. W L_{III}-edge and Zr K-edge data were collected as a function of temperature from 5 to 350 K.

The sample used in this experiment was a ZrW_2O_8 powder, which was prepared from high-purity Alfa AESAR Puratronic grade ZrO_2 (99.978%) and WO_3 (99.998%) in a stoichiometric ratio. The powders were vibratory milled in methyl ethyl ketone to reduce the particle size. After drying, the powder mixture was uniaxially pressed into pellets and heated in an oxygen atmosphere to 1470 K for 4 h and quenched to room temperature. The sample was reground and passed through a 400-mesh sieve to obtain a fine powder. The fine powder was then brushed onto Scotch tape in order to make samples for XAFS measurements.

III. XAFS DATA AND ANALYSIS

A. XAFS data

The x-ray-absorption data were reduced using standard procedures.[15,16] The XAFS k-space data are shown in Fig. 2 for the W L_{III} and Zr K edges at 20 K. Both sets of data show very good quality. Here k is the wave vector and χ is the XAFS function, which is defined as $\chi = (\mu - \mu_0)/\mu_0$, where μ is the absorption coefficient and μ_0 is the background (embedded atom) function.[17]
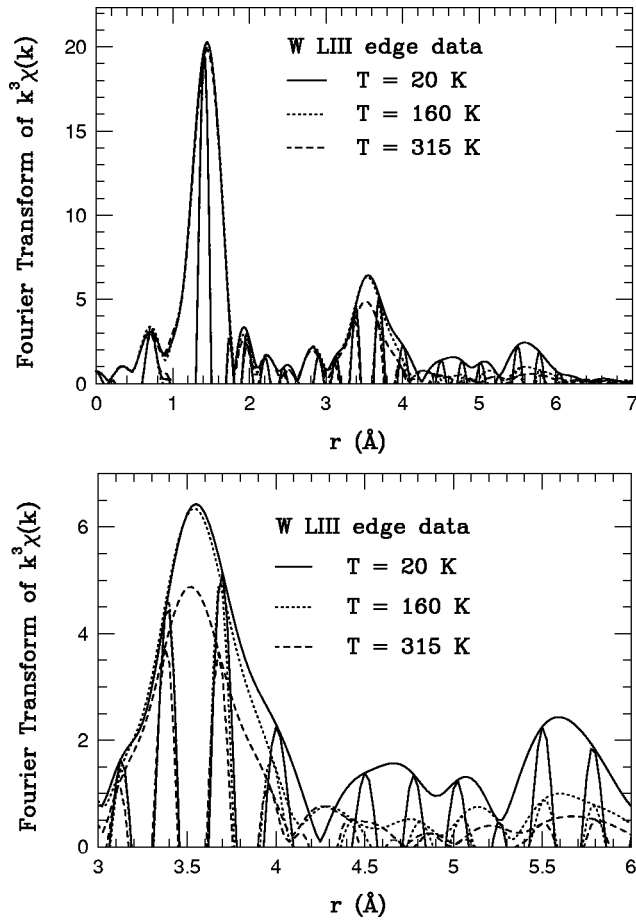
FIG. 3. The Fourier transform (FT) of $k^3\chi(k)$ of the W L_{III} edge, at 20, 160, and 315 K. The FT range is $3.3 \sim 13.5$ Å^{-1}, with 0.3-Å^{-1} Gaussian broadening. The curve with a high frequency inside the envelope is the real part of the FT (FT$_R$). The envelope is defined as $\pm\sqrt{FT_R^2 + FT_I^2}$, where FT$_I$ is the imaginary part of the FT. The upper panel shows the data range from 0 to 7 Å, while the lower panel is an expanded view from 3 to 6 Å to show the detailed changes in r space.

XAFS r-space data [the Fourier transform (FT) of the k-space data] are shown in Fig. 3 for the W L_{III}-edge data. The r space data show peaks which correspond to different atomic shells around the central atom. The position of each peak is shifted slightly in r space as a result of a well-known phase shift. The temperature dependence of each peak provides information about the relative (correlated) vibrations of the corresponding atomic shell. A reduced amplitude of a peak indicates a larger width, σ, and hence a larger local distortion of that atomic shell. Detailed discussion about the XAFS technique and data analysis can be found in Refs. 15–19.

The FT of $k^3\chi(k)$ is plotted in Fig. 3 instead of $k\chi(k)$ to enhance the change in the amplitude of peaks at longer distance (from 3 to 6 Å). The upper panel shows that the first W-O peak (at ~ 1.4 Å) has very little temperature dependence, which indicates that the W-O bonds in the WO$_4$ tetrahedra [for both W(1) and W(2)] are very rigid and essentially undistorted as the temperature increases to 315 K. In the expanded view (lower panel of Fig. 3), the peak near 3.5
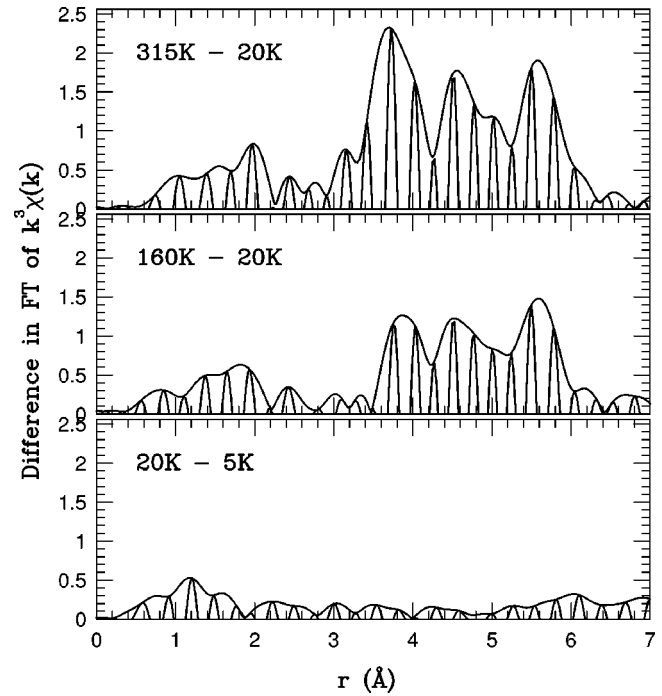

FIG. 4. The difference in r-space data for the W L_{III}-edge data for various temperatures. Data were obtained by subtracting one data file from another. Note the small difference for the first two peaks (up to 3.3 Å) compared to the large difference for the more distant peaks (3.5~5.8 Å).

Å, corresponding to the W-Zr atom pair, also shows little change in the amplitude from 20 to 120 K, while the amplitude of this peak drops about 25% when the temperature reaches 315 K. In contrast, the peak near 4.0 Å, which is mainly due to the nearest W$_1$-W$_2$ atom pair, changes about 60% from 20 to 315 K. This much larger amplitude decrease with temperature near 4.0 Å indicates that the vibrations between the nearest W(1) and W(2) are much softer than that between the nearest W-Zr atom pair. These soft vibrational modes can be excited at much lower temperatures. The peak near 5.6 Å includes several single- and multiple-scattering peaks, and also has a large change in amplitude with temperature.

To show the temperature dependence more clearly, difference data are shown in Fig. 4. These plots are the difference in the FT of $k^3\chi(k)$ data between 20 and 315 K, 20 and 160 K, as well as 20 and 5 K. Figure 4 clearly illustrates that significant changes only occur beyond 3.5 Å as the temperature is increased. The bottom panel indicates almost no change to 20 K; the middle panel shows little change up to 3.5 Å, however, several significant peaks near 3.9, 4.5, 5.0, and 5.6 Å appear. This indicates that large local distortions for atom shells at these distances are present at 160 K. These distortions become even larger when the temperature is increased to 315 K as indicated in the top panel. An additional contribution develops near 3.6 Å for T at 315 K, which is due to a change in the amplitude for the W-Zr peak. A small peak also develops at 2 Å (see top panel of Fig. 4); it arises from a large change in the fluctuations of the long W(1)-O(3) distance between the two WO$_4$ tetrahedra.
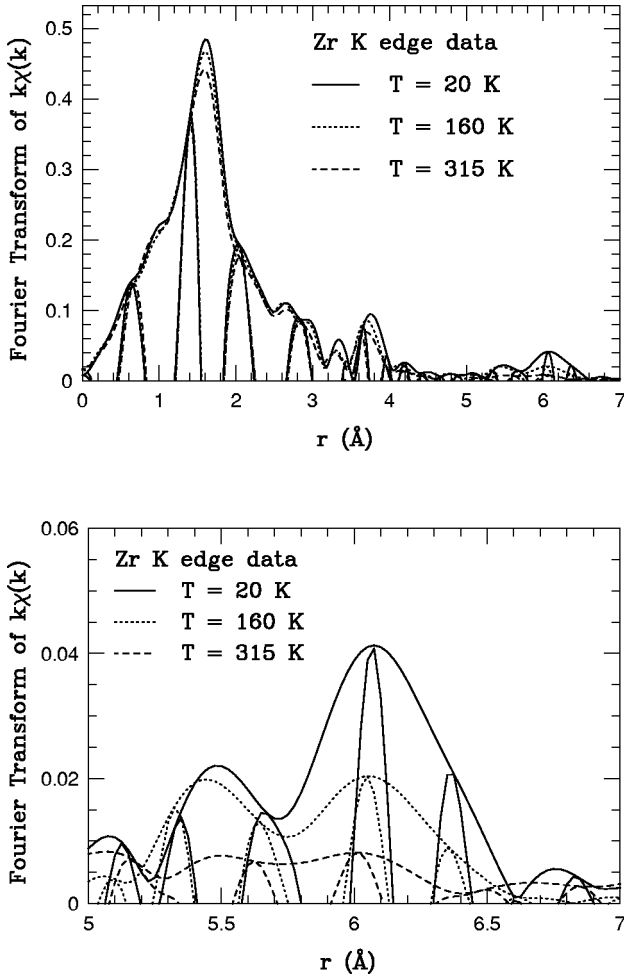
FIG. 5. Fourier transform of $k\chi(k)$ for Zr K-edge data at 20, 160, and 315 K, respectively. The FT range is 3.5–13.5 Å^{-1}, with 0.3-Å^{-1} Gaussian broadening. The lower panel is an expanded view of the data from 5 to 7 Å.

The r-space data for the Zr K edge are shown in Fig. 5. The first peak near 1.6 Å is the nearest Zr-O peak, and shows a small change with temperature ($\sim 10\%$ from 20 to 315 K). The Zr-W peak is near 3.7 Å in this plot, and the change in the amplitude is about 20% as temperature increases from 20 to 315 K. This result is quite close to that obtained in analyzing the W L_{III}-edge data. The largest change is at a long distance (around 6 Å), where the Zr-Zr peak occurs. The lower panel shows the details of the data at large r. There is a peak near 5.5 Å which also has a large change with tem-

TABLE I. Near-neighbor atom-pair distances calculated from neutron powder-diffraction data at 300 K (Ref. 21).

Atom pair	Distances (Å)
W-O	1.708, 1.807, 1.718, 1.785, 2.410
W-Zr	3.745, 3.870
W-W	4.128
Zr-O	2.034, 2.095
Zr-Zr	6.455, 6.484

perature. However, there are several multiple-scattering contributions to this peak and the analysis is more complicated. The Zr-Zr peak at 6.0 Å changes over 75% with temperature (from 20 to 315 K), which is a surprisingly large effect.

B. Fitting procedures

The XAFS equation we use is given by

$$k\chi(k) = \sum_i k\chi_i(k)$$

$$= \text{Im} \sum_i A_i \int_0^\infty F_i(k,r) \frac{g_i(r_{0i},r)e^{i[2kr+2\delta_c(k)+\delta_i(k)]}}{r^2} dr, \tag{1}$$

where χ_i is the XAFS function for shell i, $F_i(k)$ is the backscattering amplitude of the photoelectron from neighbors i (it includes mean-free-path effects), $g_i(r_{0i},r)$ is the pair distribution function for the atoms at a distance r_{0i}—assumed to be Gaussian for most of this work—and $\delta_c(k)$ and $\delta_i(k)$ are the phase shifts of the central and backscattered photoelectron waves. The amplitude factor A_i is given by

$$A_i = N_i S_0^2, \tag{2}$$

where N_i is the number of equivalent atoms in shell i, and S_0^2 is the effective "amplitude reduction factor" that accounts primarily for many-body effects such as shake-up or shake-off, but also includes small corrections to the mean free path in the theoretical functions. In this equation, the photoelectron wave vector k is defined by $k = \sqrt{2m_e(E-E_0)/\hbar^2}$, where E_0 is the binding energy for the absorption edge under study.

A detailed fit was carried out for W L_{III}- and Zr K-edge data in r space using theoretical functions for χ_i calculated using the FEFF7 code, which has been developed by Zabinsky and co-workers.[20] S_0^2 was found to be 0.99 for the W L_{III}-edge and Zr K-edge data. Each peak in the r-space data was fit with a Gaussian distribution function, and the width of this function, σ, was extracted. σ, also called the Debye-Waller factor, is a measure of the local distortions of a shell of neighboring atoms. The fit range is 1.0–5.8 Å for the W L_{III}-edge and 1.2–6.2 Å for the Zr K-edge data.

Details about the crystal structure can be found in Refs. 21 and 25. Briefly, each $W(1)O_4$ tetrahedron (gray areas in Fig. 1) is surrounded by three O(1) and an O(4)—the latter is located on a $\langle 111 \rangle$ axis; each $W(2)O_4$ tetrahedron (black areas in Fig. 1) is surrounded by three O(2) and an O(3) [O(3) is also located on the $\langle 111 \rangle$ axis]. Therefore there are four short W-O bonds [W(1)-O(1), W(1)-O(4), W(2)-O(2), and W(2)-O(3)] distributed from 1.7 to 1.8 Å (see Table I) plus one long bond at 2.41 Å [W(1)-O(3)]. However, XAFS cannot differentiate between W_1 and W_2 in this material and it is impossible to distinguish such small distances between the nearest W-O bonds. Therefore the theoretical standard for the first W-O peak in r space is a sum of the peaks for the four short W-O bonds, and the bond distance is averaged to be 1.7752 Å. Since all W-O bonds within one WO_4 tetrahe-

dra are included in this standard, it is easy to tell whether the bonds within the tetrahedra became distorted as the temperature increases. The octahedra surrounding each Zr are composed of three O(1) and three O(2), so that the theoretical standard for the nearest Zr-O peak in r space includes two Zr-O bonds, at 2.03 Å [Zr-O(1)] and 2.09 Å [Zr-O(2)], due to similar constraints.

In extended XAFS (EXAFS) analyses the maximum number of parameters is given by[22]

$$P_{max} = \frac{2\Delta k \Delta r}{\pi} + 2, \tag{3}$$

where Δk is the Fourier-transform k range and Δr is the fitting r range. From the above discussed k and r ranges, P_{max} corresponds to 33 and 34 parameters for the W L_{III}- and Zr K-edge data, respectively. To minimize the number of parameters used, the peaks for distances that are nearly the same are summed as described above. In addition, the number of neighbors in each shell/multiple-scattering path is constrained from the known crystal structure.

In our fitting procedure, 12 theoretical standard peaks were used to fit the W L_{III}-edge data. These 12 include the nearest W-O peak (combination of all four nearest W-O bonds), the W-Zr peak (combination of both single- and multiple-scattering effects), the nearest and second-nearest W-W peaks, plus eight other multiple-scattering peaks with smaller amplitudes. For the Zr K-edge data, eight theoretical standard peaks were used in the fit. They include the nearest Zr-O peak (a combination of the two short Zr-O bonds), the Zr-W peak (combination of both single- and multiple-scattering effects), the nearest Zr-Zr peak (combination of the two shortest Zr-Zr atom pairs), and five other multiple-scattering peaks with small amplitudes.

There are in general four parameters associated with each peak: σ, Δr, amplitude, and ΔE_0 [there can also be higher cumulants, C_3 (asymmetry) and C_4 (kurtosis); these are discussed in the following paragraph]. σ is the width of the pair distribution function (PDF), Δr is the change of the bond (atom-pair) distance from the starting value, the amplitude is a measure of S_0^2 [see Eq. (2)], and ΔE_0 is a shift of the absorption binding energy. An initial step, for both the W L_{III} and Zr K edges, was to determine the amplitude and ΔE_0 for each peak using low-temperature data for which the signal-to-noise ratio is highest. In subsequent fits of the data at various temperatures, S_0^2 and ΔE_0 were fixed, and Δr and σ were allowed to vary. In order to further reduce the total number of free parameters during fitting the W L_{III}-edge data, only Δr's for the single-scattering peaks—the nearest W-O and W-Zr, and the nearest and second-nearest W-W peaks—were allowed to vary; the Δr's for the eight small multiple-scattering peaks were determined at low temperature and fixed. Note that the small thermally induced changes in Δr for these contributions, estimated from the known thermal contraction, are $\leqslant 0.015$ Å. This is at most comparable to the error in Δr for these small peaks. Allowing these Δr's to vary from the low-T values did not significantly improve the quality of the fit parameter. For the Zr K-edge fit, Δr was allowed to vary for all peaks. As a result, the number of free

TABLE II. Scattering paths between W and Zr as well as the nearest W-W pair. Paths with only two atoms involved are single-scattering paths, i.e., the photoelectron wave is directly backscattered from another atom. Paths involving more than two atoms are multiple-scattering paths.

Path	Degeneracy	Path distance (Å)
W_1-Zr	3	3.745
W_2-Zr	3	3.870
W_1-O-Zr	6	3.793
W_2-O-Zr	6	3.875
W_1-O-Zr-O	3	3.841
W_2-O-Zr-O	3	3.880
W_1-W_2	1	4.128
W_1-O-W_2	2	4.128
W_1-O-W_2-O	1	4.128

parameters in the fit procedure is 16 for both edges, much less than P_{max} mentioned above.

A few fits were also carried out in which the C_3 or C_4 parameter was varied for the W-O, Zr-O, W-W, and Zr-Zr peaks. C_4 fluctuated in sign and its average value was close to zero. C_3 was slightly negative for W-O ($\sim -4.0 \times 10^{-5}$ Å^3), and positive and slightly larger in magnitude for Zr-O (~ 0.00016 Å^3), but with little temperature variation. The C_3 results for Zr-O suggests that this bond expands asymmetrically with T. For W-W, C_3 is negative and increases in magnitude with T (from $-3E-5$ to -0.0006 Å^3 as temperature increases from 5 to 315 K), however, the errors are large, about 0.0003 Å^3 at 315 K, because of the overlap of this peak with the W-Zr peak, and the effect is small below 300 K.

In the following fits, the theoretical standards for W-Zr (Zr-W) are a sum of both the W-Zr (Zr-W) single scattering and the W-O-Zr (Zr-O-W) multiple scattering since the theoretical standards overlap in r space and have similar distances. The same procedure was used to obtain the theoretical standard for the W(1)-W(2) atom pair. See Table II for detailed information about all the single and multiple paths. In these fits the amplitude NS_0^2 was kept constant to reduce the relative error in σ^2. Absolute errors in S_0^2 are of order 10% and shift the σ^2 vs T plots vertically. The error bars show the relative error; several traces are collected at each temperature and analyzed independently. The error bars indicate the rms variation in the values of σ^2 obtained at each temperature.

Figure 6 shows σ^2 as a function of temperature. In the upper panel, σ^2 for the nearest W-O bond is nearly independent of temperature—the WO$_4$ tetrahedra are very rigid up to 315 K. The small change in σ^2 with temperature for the nearest Zr-O peak (Fig. 6, bottom panel) shows that the ZrO$_6$ octahedra are not rigid although quite stiff within this temperature range.

The σ^2 curves for W-Zr (black square in Fig. 6, upper panel) and Zr-W (black square in Fig. 6, bottom panel) are nearly parallel with only a tiny vertical shift between each other. This is not surprising because both curves measure the
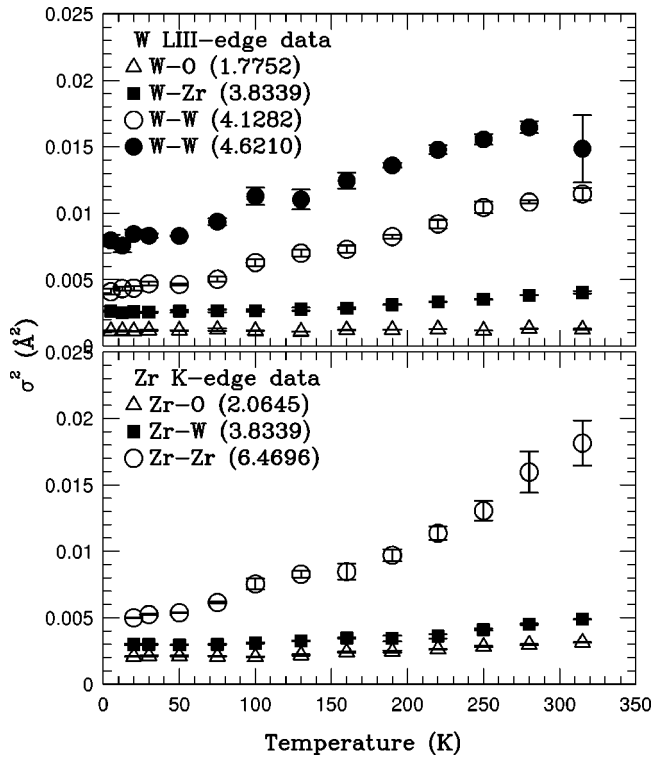
FIG. 6. σ^2 vs temperature for the W L_{III}-edge data (upper panel) and the Zr K-edge data (lower panel). The error bars are about the size of the symbol except for a few data points indicated in the plot.

FIG. 7. A comparison of the temperature dependence of σ^2 for the W-Zr, Zr-W, and Zr-O peaks. σ^2_{Zr-W} and σ^2_{Zr-O} are shifted slightly to make the curves overlap at low temperatures. The high-temperature data for σ^2_{W-Zr} and σ^2_{Zr-W} have a small difference since data were collected on two distinct edges. The difference between σ^2_{W-Zr} (σ^2_{Zr-W}) and σ^2_{Zr-O} is a rough measure of the contribution made by the transverse vibration of the middle O atom in the W-O-Zr linkage. Note that the three sets of data overlap within the error bars up to ~220 K.

same local structure from two different perspectives. The very small vertical shift comes from the fit procedure and the different edges. In Figure 7, we show on an expanded scale that the temperature dependence of σ^2 for the Zr-W and W-Zr peaks are essentially the same and only slightly larger than that for the Zr-O peak.

Another fit was carried out, in which the σ's for the single- and multiple-scattering peaks were fit separately for the W-Zr atom pair; the fit result shows that σ^2 for each contribution is about the same (see Fig. 8). However, the data do not support further attempts to extract separate σ's for the W(1)-Zr and W(2)-Zr single- and multiple-scattering peaks (i.e., a fit of four independent peaks) because these peaks are too close together and there would be too many free parameters for this r range.

It is surprising that σ^2 for the W-Zr (Zr-W) pair shows only a small temperature dependence, comparable to that for the nearest Zr-O bond. This indicates that the nearest W-O-Zr linkage is quite stiff—the W-Zr distance does not fluctuate much with temperature up to 300 K, although the distance between the nearest W and Zr atoms is more than 3.7 Å with an oxygen in between. In contrast, the nearest W-W pair [a W(1)-W(2) pair along a ⟨111⟩ direction] with only a slightly longer pair separation, 4.128 Å, shows a much larger temperature dependence of σ^2, as does the second-nearest W-W pair [also a W(1)-W(2) pair at 4.621 Å]. The change in σ^2 with temperature for W-W is more than five times larger than that for the W-O-Zr linkage. The nearest Zr-Zr atom pair has the largest change in σ^2 with temperature. Note that the
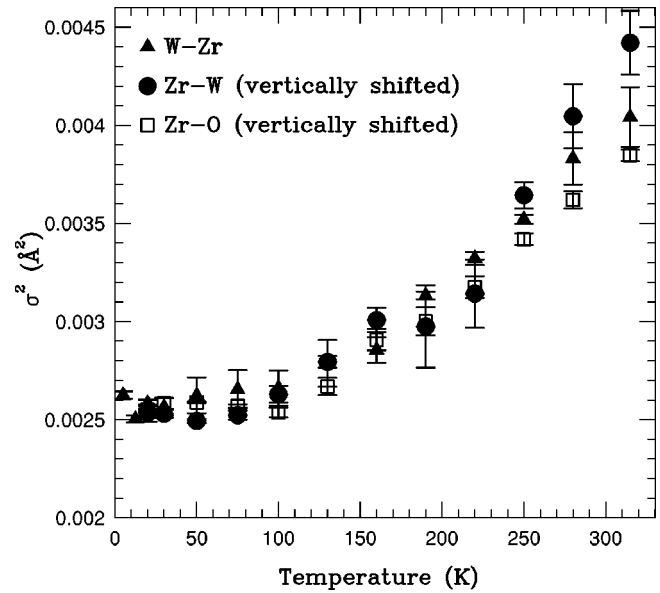
much larger error bars for the Zr-Zr peak (Zr K-edge data) at high temperature are due to the weak XAFS signal for peaks with a large σ at large distances (near 6.5 Å). The amplitude of the Zr-Zr peak at high temperature (above 280 K) is approaching the noise level. Error bars for σ^2 in this temperature range are quite large for the W-W and Zr-Zr pairs as indicated in Fig. 6.

An important feature of Fig. 6 is that the σ^2 curves for both nearest and second-nearest W-W pairs are almost paral-
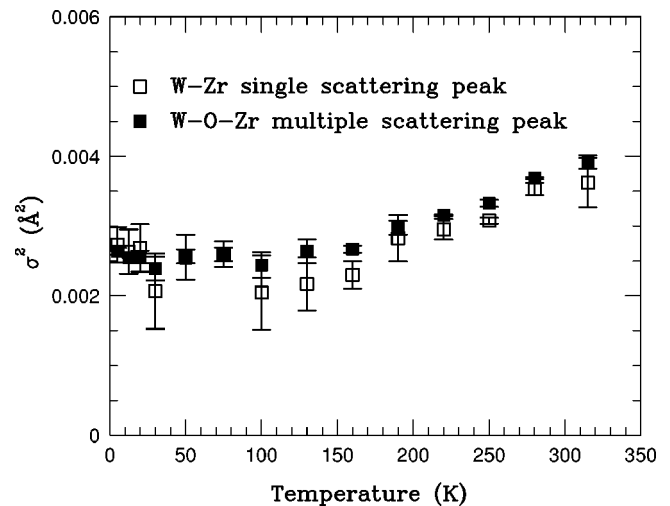

FIG. 8. σ^2 vs temperature for both the W-Zr single-scattering and W-O-Zr multiple-scattering peaks.

TABLE III. Estimated Einstein temperatures for each mode.

Atom pair	Θ_E (K)
W-O	962(50)
Zr-O	493(50)
W-Zr	470(50)
Zr-W	459(50)

lel, which indicates correlated vibrations between these two sets of atom pairs. A break point or cusp clearly exists for both plots near 100 K. Furthermore, the temperature dependence of σ^2 for the Zr-Zr pair is also similar, with the same break point present near 100 K. To check that this is not an artifact, a second data set was collected for each edge as a function of temperature; the data yield the same result. A detailed discussion of the interpretation of this break point will be given in the next section.

IV. ADDITIONAL ANALYSIS AND DISCUSSION

A. Einstein temperatures

The specific-heat measurements of Ramirez and Kowach show that low-energy Einstein modes (Einstein temperatures, $\Theta_E \sim 38$ and 67 K) associated with optical phonons dominate and are overwhelmingly responsible for NTE in this material.[10] Similar results were also obtained by phonon density-of-states measurements[3,11] and theoretical simulations.[12,13] However, the calculations suggest a larger contribution for low-frequency transverse-acoustic modes than had been assumed in the experiments. To have a large contribution to NTE, the entire band of such transverse-acoustic modes must be below ~ 8 eV.

In crystals, the temperature dependence of σ^2 for optical modes can be modeled with a sum of Einstein contributions:[18]

$$\sigma^2 = \frac{\hbar^2}{2M_R k_B \Theta_E} \coth \frac{\Theta_E}{2T}, \tag{4}$$

where M_R is the reduced mass and k_B is Boltzmann's constant. The high-temperature approximation (when $\Theta_E/T \leq 0.3$) of Eq. (4) can be written as

$$\sigma^2 = \frac{\hbar^2 T}{M_R k_B \Theta_E^2}. \tag{5}$$

Thus we can extract an estimate of the Einstein temperature for vibrations of various atom pairs from the σ^2 vs T plots (Fig. 6) for the purpose of comparing with the specific-heat results (for the W-O and Zr-O peaks, a Debye approximation is normally a better model). The results are given in Table III for the three nearest atom pairs. All Θ_E are larger than 450 K; in particular, Θ_E for the W-Zr pair is comparable to that for the Zr-O bond. This is another way of quantifying that the W-Zr pair distance is very stiff. The high Einstein temperature for W-Zr (Zr-W) means that the vibration of O in the W-O-Zr linkage does not correspond to the low-frequency modes observed in the heat-capacity measure-
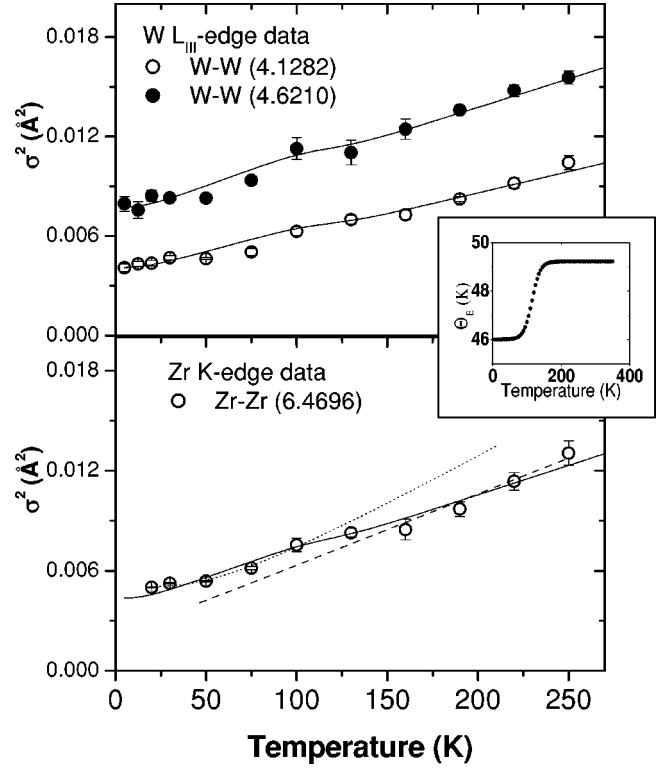

FIG. 9. Fit results to σ^2 vs T data for the W-W and Zr-Zr atom pairs. The solid lines are the fit results and were carried out up to 250 K because the data at higher temperatures have very large error bars. The temperature dependence of Θ_E is plotted in the inset of the figure. The dotted and dashed lines in the bottom panel are the fit results for a fixed Θ_E at low T (dotted) and high T (dashed).

ments. Results of the Einstein temperature for the W-W and Zr-Zr pairs are discussed in the next subsection.

B. Further identification of the low-energy modes in ZrW$_2$O$_8$

The low-energy phonon density of states determined by Ernst et al.[11] show that the lowest mode frequency remains unchanged as temperature increases from 50 to 100 K but clearly increases (hardens) by 7% between 100 and 300 K as shown in Fig. 3 of Ref. 11. This means that the effective spring constant κ must increase significantly. Such a change should be observed in XAFS data if the atomic displacements are driven by this mode since at high temperature

$$\sigma^2 \sim k_B T/\kappa \tag{6}$$

within the Einstein approximation (note that κ is proportional to Θ_E^2).

Of all the plots of σ^2 vs temperature (see Fig. 6) only the data for the W-W and Zr-Zr atom pairs show an anomaly between 100 and 300 K—both show a cusp just above 100 K, and the temperature dependence of σ^2 becomes slower. The nature of this feature is shown in more detail for the Zr-Zr data in Fig. 9, where separate Einstein fits are made for the low-T ($I < 100$ K) and high-T(>150 K) data. The step clearly occurs between 100 and 150 K. This is very unusual behavior, but is exactly the result expected if the effective

TABLE IV. The fit results with temperature dependent Θ_E using Eq. (4) and Eq. (7). In these final fits, T_0 and δ in Eq. (7) were fixed at 115 and 12 K, respectively.

Atom pair	Reduced mass (g/mol)	Θ_{E0} (K)
W-W (4.1282 Å)	750(50)	46(10)
W-W (4.6210 Å)	550(50)	47(10)
Zr-Zr (6.4696 Å)	580(50)	46(10)

spring constant were to increase just above 100 K. To represent this mode hardening we define Θ_E to be a function of temperature:

$$\Theta_E = \Theta_{E0} + 0.07 \times \Theta_{E0} \times \left[1 - \frac{1}{e^{(T-T_0)/\delta} + 1} \right]. \quad (7)$$

Here, Θ_{E0} is the Einstein temperature at low T. T_0 is the temperature at which Θ_E increases, and δ is the width of this step function. We used the small 7% mode hardening as reported by Ernst et al.,[11] and found T_0 and δ to be $\sim$115 K and 12 K to fit the data. Θ_E at low temperature is $\sim$ 46 K for the W-W and Zr-Zr pairs (see Table IV for details) consistent with the heat-capacity and phonon measurements. The fit results are reasonable as shown in Fig. 9, where solid lines are the fit results and the circles are the data. Θ_E as a function of temperature is shown in the inset. Separate fits to the low-T and high-T parts of the σ^2 vs T curve show that the average static distortion, σ^2_{static}, is very large for the W-W and Zr-Zr atom pairs (0.0032 Å^2 for the nearest W-W, 0.0069 Å^2 for the second-nearest W-W, 0.0034 Å^2 for the nearest Zr-Zr). We therefore use these values of the static distortions in the overall fit for each atom pair, respectively. The fit results in Table IV show very large reduced masses for these modes compared to the W-O or Zr-O reduced masses used in Table III. This indicates that the low-energy vibration modes must involve several large rigid units which include the heavy metal atoms, W and Zr. Part of the reason for the very large value of the reduced mass in this fit is that we have used an equation for a single type of mode; in fact we should sum over the four lowest modes that are clearly present from the specific-heat analysis. To do so we would need the projections of the phonon modes onto the W motions along the $\langle 1,1,1 \rangle$ directions. A crude approximation is that Eq. (4) should be multiplied by a number between 1.5 and 2.5; then M_R is about 350 g/mol for W-W, which is still very large. The clear indication of a small hardening of the effective spring constant for only the W-W and Zr-Zr pairs completes our identification of the low-energy modes in this system as being vibrations of W(1)-W(2) along the $\langle 111 \rangle$ axes, which are coupled to the Zr-Zr motions as described below.

An unanswered question is why does the mode harden near 100 K? The answer may be related to the amplitude of the W-W vibration. For small amplitudes, nearly rigid unit modes may be possible at low temperature with only a small flexing about the O atoms that connect the WO$_4$ and ZrO$_6$ units. However, at larger amplitudes, the angles within the
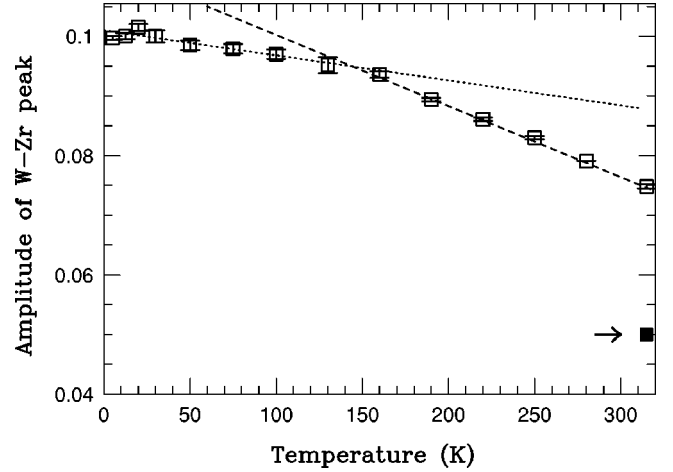

FIG. 10. The W-Zr peak amplitude obtained from the W L$_{III}$-edge data. The dotted line has a very small slope, which shows the slow amplitude decrease below 120 K. The dashed line shows the larger slope of the amplitude drop beyond 120 K. The decrease in the peak amplitude is obviously much faster as temperature increases from 160 to 315 K. The solid square (see arrow) shows where the W-Zr amplitude should be if a large transverse O vibration dominates NTE in ZrW$_2$O$_8$ as discussed in Sec. IV C.

units (i.e., the O-W-O and/or O-Zr-O angles) may also need to change slightly and the Zr-O bond to stretch, to keep the units connected; this would stiffen the vibration. A review of the supplementary data of Ref. 25 also indicates that on average the O1-W1-O1 angle decreases with temperature by roughly 0.4°, while the O2-W2-O2 decreases by 1.0° up to 293 K, which is comparable to the estimated angle change required in our tentpole model (below) for the vibration amplitudes at 300 K.

Such a possibility is also consistent with the results for the W-Zr and Zr-O peaks. As discussed earlier, σ^2_{W-Zr} changes very little below 120 K but changes rapidly at higher T. In Fig. 10, which involves no analysis, the amplitude of the W-Zr peak is plotted as a function of T. There is a break in the slope of the curve near 120 K (close to the cusp in the σ^2 vs T plots for W-W), and the amplitude decreases more rapidly for $T > 120$ K. $\sigma^2_{W-Zr}(T)$ for this peak increases too rapidly above 120 K (see Fig. 7) to fit a Debye model well. The behavior for Zr-O is similar. Although both can be fit by an Einstein model with a large Θ_E (see Table III), that is surprising since one expects these vibrations to involve the acoustic modes at these temperatures and hence to follow a Debye model. If, however, the small stretching of the Zr-O bond (and the transverse O motion, see Sec. IV C 2) is a by-product of low-energy Einstein modes, driven by the large inertia of the massive WO$_4$ tetrahedra, then the simple Einstein mode equation above no longer applies—the resulting Zr-O vibration amplitude would be much smaller than expected for a low Θ_E. Within this model the Zr-O bond begins to fluctuate and the O to move transversely at a low frequency once the W amplitude reaches a critical value (near 120 K).

C. Transverse vibration of O in W-O-Zr

The above results show that the temperature dependence of the W-Zr pair (and W-O-Zr) is weak. Because the origin

of the NTE effect in ZrW_2O_8 has long been thought to be a large-amplitude low-energy transverse vibration of the O atom in the middle of the W-O-Zr linkage,[2] we address the analysis of the W-Zr peak in more detail. The results depend on assumptions about the atomic correlations; we consider uncorrelated and correlated situations separately.

1. Uncorrelated motions

We first note that if the transverse O vibration in the W-O-Zr were solely responsible for the NTE of 9×10^{-6} K in ZrW_2O_8, the required O vibration would need to have an rms transverse displacement of at least 0.15 Å ($\sigma^2 \sim 0.02$ Å^2) to produce the observed thermal contraction at 300 K.[7] Here both the W-O and Zr-O bonds are assumed to be rigid. Then the distance between the nearest W and Zr atoms must fluctuate significantly (Fig. 11). For example, the W(1)-Zr pair (single scattering) would have a contribution to σ^2 of 0.003 Å^2 from this O thermal vibration, while for the W(2)-Zr pair (bond angle of 173°) the contribution to σ^2 is ~ 0.0006 Å^2. However, the total thermal change in σ^2 for the W-Zr pairs is only about 0.0015 Å^2 (Fig. 7).

More importantly, the multiple-scattering contribution to the amplitude of the W-O-Zr peak is also very sensitive to the displacement of the O atom;[19] it dominates when the bond angle is nearly colinear, since its amplitude can decrease by a factor of 3–4 when the bond angle changes from 180° to $\sim 150°$ (see upper panel of Fig. 12). For large bond angles, the single-scattering peak starts to dominate.

For W(2), the O is displaced about 0.14 Å (see Fig. 12) which corresponds to a bond angle of 173°, and in this case the multiple-scattering peak dominates. The average amplitude of the W(2)-O-Zr multiple-scattering peak is decreased by 25% as the rms oscillation amplitude of the central O atom reaches 0.14 Å. For W_1, the O displacement is ~ 0.42 Å (bond angle of 155°), and the change of the amplitude of the multiple-scattering peak is considerably smaller. In this case, the W(1)-Zr single-scattering peak is the dominant contribution.

The measured stretching vibration of the Zr-O bond must also be included in the analysis. In general, σ^2 for the W-O-Zr (or Zr-O-W) linkage can be expressed as follows when the various motions are not correlated:

$$\sigma^2 = \sigma^2_{static} + \sigma^2_{stretch} + \sigma^2_{transv}. \tag{8}$$

Here σ^2_{static} is the contribution for a static distortion, which does not have a temperature dependence; $\sigma^2_{stretch}$ is the contribution from the change in the W-Zr distance caused by a stretch of the Zr-O and W-O bonds; and σ^2_{transv} comes from the transverse vibration of the O atom in the middle of the W-O-Zr linkage. Since σ^2_{static} doesn't change with temperature, we neglect it in the following discussion. σ^2 for the W-O bond is nearly independent of temperature up to 300 K and is also neglected. Therefore, $\sigma^2_{stretch}$ can be represented by σ^2_{Zr-O}. Note that the total changes in σ^2 of the W-Zr and Zr-W peaks are about 0.0015 Å^2 and 0.0020 Å^2, respectively as the temperature increases from 5 to 315 K, while the change of σ^2_{Zr-O} over the same temperature range is about 0.0013 Å^2 (Fig. 7). The remaining contribution from the O transverse vibration, σ^2_{transv}, would not be large enough under the above assumptions to account for the total NTE in ZrW_2O_8 at 300 K. Below 100 K the changes in σ^2_{W-Zr}, σ^2_{Zr-W}, and σ^2_{Zr-O} are nearly identical, thus any O transverse oscillation must be negligible over this temperature range (see Fig. 7).

The net effect when the Zr-O stretching vibration and transverse O motions are included is that the total amplitude reduction would be too large as shown by the solid square at 315 K in Fig. 10. The open squares are the amplitudes of the W-Zr peak in the raw data and do not involve any detailed analysis. These data cannot be explained in terms of a transverse O vibration when the Zr-O bond stretches and the atomic motions are uncorrelated.

2. Correlated motions

Correlated motions of atoms occur in a variety of situations. When acoustic phonons dominate, the motions of the nearest neighbors are in the same direction—the motions are positively correlated. In more complex crystals there can be several other types of correlated motions. For example, in ZrW_2O_8 the very small value of σ^2 for the W-O bond, even at 300 K, means that the WO_4 tetrahedra move as a rigid unit—the O must follow the W motion. Similarly, although the Zr-O bond is not completely rigid, the small value of σ^2 for Zr-O indicates that the ZrO_6 octahedra are quite stiff—
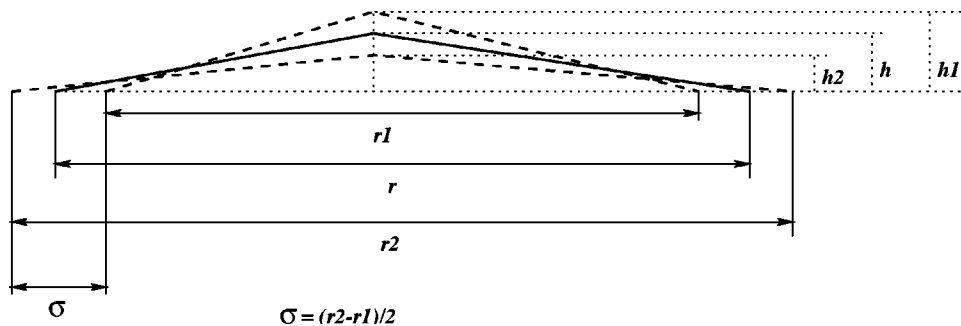

FIG. 11. This plot shows in general how the transverse vibration of the middle O atom will affect the distance between two metal (M) atoms in a M-O-M linkage for rigid M-O bonds. The solid line shows the equilibrium position, and the dotted lines show the status of the M-O-M linkage during an O transverse vibration when the O atom reaches the rms vibration amplitude at h_1 and h_2. Note σ is the half width for the M-M pair distribution function.
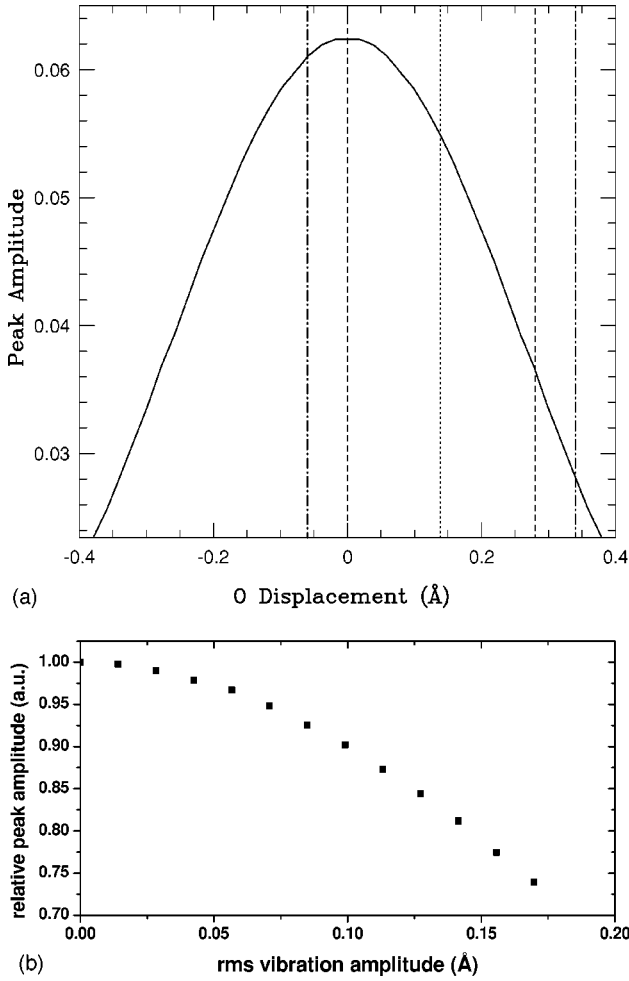
(a)

(b)

FIG. 12. The upper panel shows the multiple-scattering peak amplitude for the W-O-Zr linkage as a function of the middle O-atom displacement. The dotted line shows the equilibrium position of the middle O atom for the W(2)-O-Zr linkage. The dashed lines show the estimated rms displacement of the O at 300 K, while the dot-dashed lines show the estimated vibration amplitude. An O displacement of 0.4 Å would correspond to a bond angle ~155° for the W-O-Zr linkage. The lower panel shows the relative amplitude of the W-O-Zr multiple-scattering peak as a function of the rms value of the transverse O vibration amplitude for the W(2)-O-Zr linkage.

the O in these units must approximately follow the Zr atom. These types of correlated motions are quite common.

More surprising are the correlations within the W-O-Zr linkage in ZrW$_2$O$_8$. The small value of σ^2 for the W-O-Zr (and Zr-O-W) linkage plus the large thermal parameters observed in diffraction[2,7,25] for the O atoms indicate that the motions of the atoms in this linkage must be correlated such that the fluctuations of the W-Zr distance are small. This is a more subtle correlation in that the transverse O motion and the stretching of the Zr-O bond are not independent. An extreme case would be if the W and Zr were fixed (no length contraction) and the Zr-O bond stretched as the O vibrated transversely. Here we consider the thermally induced changes in the W-Zr distance and the rms variation of this distance under different conditions.
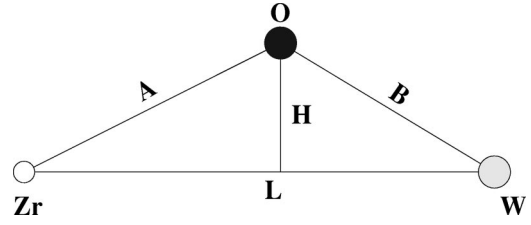

FIG. 13. A sketch of the W-O-Zr linkage to illustrate the arrangement of the atoms.

In Fig. 13 we show the arrangement of the atoms and define the parameters. Here A is the time-dependent length of the Zr-O bond, B is the length of the W-O bond which will be held constant, and H is the time-dependent transverse position of the O atom. We model the time dependencies of A and H using cosine functions:

$$A = A_o + A_1(t),$$

$$H = H_o + H_1(t), \qquad (9)$$

$$A_1(t) = a_1 \cos(\omega_A t),$$

$$H_1(t) = h_1 \cos(\omega_H t + \theta), \qquad (10)$$

where A_o and H_o are the static values, a_1 and h_1 are the vibration amplitudes, and ω_A and ω_H are the corresponding frequencies for the stretching and transverse motions. The total Zr-W distance, L, is given by

$$L = \sqrt{A^2 - H^2} + \sqrt{B^2 - H^2}. \qquad (11)$$

To simplify the final results we set $B = A_o$. Substituting for A and H, expanding the square roots to second order, and keeping terms up $A_1^2(t)$, $H_1^2(t)$, and $A_1(t)H_1(t)$,

$$L = L_o + \frac{1}{L_o}[2A_o A_1(t) + A_1^2(t) - 4H_o H_1(t) - 2H_1^2(t)]$$

$$- \frac{1}{L_o^3}[4A_o^2 A_1^2(t) + 8H_o^2 H_1^2(t) - 8A_o H_o A_1(t)H_1(t)],$$

$$(12)$$

where $L_o = 2\sqrt{A_o^2 - H_o^2}$. Next we need to calculate the average length change $\langle \Delta L \rangle = \langle L - L_o \rangle$ and its variance, $\sigma_{thermal}^2 = \langle (\Delta L)^2 \rangle$, which would correspond to $\sigma_{stretch}^2 + \sigma_{transv}^2$ in the previous section. To calculate these averages, we need to know how $A_1(t)$ and $H_1(t)$ are correlated. Using Eq. (10) we show that

$$\langle A_1(t) \rangle = \langle H_1(t) \rangle = 0,$$

$$\langle A_1^2(t) \rangle = a_1^2/2; \quad \langle H_1^2(t) \rangle = h_1^2/2, \qquad (13)$$

and

$$\langle A_1(t)H_1(t) \rangle = \int A_1(t)H_1(t)dt. \qquad (14)$$

If $\omega_A \neq \omega_H$, then $\langle A_1(t)H_1(t) \rangle = 0$; for $\omega_A = \omega_H = \omega$,

$$\langle A_1(t)H_1(t)\rangle = \frac{1}{T}\int_0^T h_1 a_1 \cos(\omega t)\cos(\omega t + \theta)dt = \frac{h_1 a_1 \Phi}{2},$$

$$(15)$$

where $\Phi = \cos\theta$ is called the correlation parameter and can vary from -1 to 1. After simplification,

$$\langle \Delta L \rangle = -\frac{1}{L_o(A_o^2 - H_o^2)}[A_o^2 h_1^2 + H_o^2 a_1^2/2 - A_o H_o a_1 h_1 \Phi]$$

$$(16)$$

and

$$\sigma^2_{thermal}(\Phi) = \frac{2}{L_o^2}[A_o^2 a_1^2 + 4H_o^2 h_1^2 - 4A_o H_o a_1 h_1 \Phi].$$

$$(17)$$

If A_1 and H_1 are uncorrelated this reduces to

$$\sigma^2_{thermal}(0) = \frac{A_o^2}{2(A_o^2 - H_o^2)}\left[a_1^2 + 4\frac{H_o^2}{A_o^2}h_1^2\right],\qquad (18)$$

while for positively correlated motions

$$\sigma^2_{thermal}(1) = \frac{A_o^2}{2(A_o^2 - H_o^2)}\left[a_1 - 2\frac{H_o}{A_o}h_1\right]^2.\qquad (19)$$

Under the assumption that a_1 is very small (i.e., Zr-O is rigid), $\langle \Delta L \rangle \sim -h_1^2/L_o$, as used earlier to estimate the magnitude of the transverse vibration amplitude required to produce a Zr-W length contraction corresponding to the bulk value. When a_1 is finite and the motions correlated ($\Phi > 0$) then the net contraction is smaller. However, for the value of a_1 obtained from σ_{Zr-O} at 300 K ($a_1 \sim 0.08$ Å), this correction is small, $\sim 8\%$.

In contrast, the effects of correlations on $\sigma^2_{thermal}(\Phi)$ are large. Using $a_1 \sim 0.08$ Å, $h_1 = 0.21$ Å, $H_o = 0.4$ Å for W(1)-O-Zr, and $A_o \sim 2$ Å, then $\sigma^2_{thermal}(0) \sim 7.0 \times 10^{-3}$ Å^2, while $\sigma^2_{thermal}(1) \sim 8.3 \times 10^{-6}$ Å^2. Thus $\sigma^2_{thermal}(\Phi)$ can have a wide range of values depending on the value of Φ.

In the above discussion we have used a value of h_1 obtained from the oxygen thermal parameters in diffraction experiments. This is an overestimate of the transverse motion, since part of the O displacement must correspond to the rotations/translations of the W-O-Zr linkage (which includes translations of the WO$_4$ and ZrO$_6$ units). Ideally a determination of Φ would provide a measure of the transverse motion within the W-O-Zr linkage. However, in Eq. (17), Φ and h_1 are coupled. An approximate determination can be obtained by using the results of the fits for the W-O-Zr linkage to the sum of the single-scattering and multiple-scattering peaks as shown in Fig. 8. Using the effective value of σ^2 obtained for W-O-Zr at 300 K, the dominant W(2)-O-Zr multiple-scattering peak amplitude should drop by $\sim 25\%$ from 20–300 K. Using the measured value of σ^2 for the Zr-O component accounts for 17%–20% of this drop, leaving 5%–8% from changes in the multiple-scattering peak as a result of the transverse vibration. From Fig. 12, lower

panel, this yields rms values ($h_1/\sqrt{2}$) for the transverse O motion (within the linkage) of 0.067–0.092 Å, considerably smaller than the total O motion determined from the diffraction thermal parameters.

D. Possible transverse motions of O(3) in W(1)-O(3)-W(2) linkage

In the above discussion, we showed that for a nearly colinear three-atom linkage, the amplitude of the multiple-scattering XAFS peak is strongly dependent on transverse vibrations of the middle atom. Since O(3) is located between W(1) and W(2), we need to consider the same possibility for the W(1)-O(3)-W(2) peak. If the transverse vibration of O(3) dominates, there should not be a large W motion. However, the second-nearest W-W pair also has a very large change in σ^2 with temperature and there is no atom between this pair. This suggests that it is the W atom that is moving significantly rather than the transverse motion of the O(3).

Another way to address the question is to look at the temperature-dependent broadening of σ for the long W(1)-O(3) pair. Because the W-O bonds within the tetrahedra are very rigid, the change of σ^2 for the W(1)-W(2) pair must be comparable to that for the W(1)-O(3) if transverse oscillations of O(3) are not large. Although the W(1)-O(3) peak is difficult to observe in the regular data because it has an amplitude of $\sim 1/15$ for the short W-O bond,[23] it is clearly observed in the difference data of Fig. 4; a peak develops at 2 Å for the difference data between 20 and 315 K. The amplitude for the main W-O peak in the difference data is about 40% smaller. In order to estimate the broadening of the W(1)-O(3) peak with temperature, we used a method of fitting r-space difference data recently developed in our magnetic-field modulation experiments.[24]

Briefly, this method is as follows. The XAFS function $\chi(k)$ can be written as

$$k\chi(k) = \sum_i e^{-2\sigma_i^2 k^2}\text{func}(k, r_i) = \sum_i k\chi_i.\qquad (20)$$

Here r_i is the distance from the central atom to the ith atom shell; k is the wave vector and σ_i is the width of the PDF of the ith atom shell. Note func(k, r_i) is a function which has no σ_i term in it. Assuming σ_i is the only parameter changing with temperature (r_i also varies with T, but is a very small effect compared to the change in σ_i), then we get[24]

$$\delta[k\chi_i(k)] = -4\sigma_i \delta\sigma_i k^3 \chi_i(k).\qquad (21)$$

Thus the amplitude in the difference data is proportional to $\delta\sigma_i$. The r-space data for the W L_{III} edge is the Fourier transform of $k^3\chi(k)$ data. Let σ for the W(1)-O(3) peak be σ_{20} at 20 K and σ_{315} at 315 K, where $\sigma_{315} = \sigma_{20} + \delta\sigma$. Then we have the difference, $\delta(k^3\chi)$:

$$k^3\chi(k)(315\text{ K}) - k^3\chi(k)(20\text{ K}) = -4\sigma_{20}\delta\sigma[k^5\chi(k)].$$

$$(22)$$

We generated a $k^5\chi(k)$ standard for the W(1)-O(3) peak to fit the difference data of $k^3\chi(k)$. The fit procedure is the same as a normal r-space fit. Once we extract the amplitude

of the peak from the fit, we can obtain $\delta\sigma$, the increase of σ with temperature. The result of the fit shows that $\delta\sigma$ is ~ 0.045 Å, and $\sigma^2_{315} - \sigma^2_{20} \sim 0.005$ Å^2 which is close to the σ^2 change for the nearest W-W peak, ~ 0.0065 Å^2, over the same temperature range. Such a large change in σ^2 with temperature for the W(1)-O(3) peak confirms that the W (and hence the rigid WO$_4$ tetrahedra) has significant translations along a $\langle 111 \rangle$ axis, in agreement with the large value of σ^2 for the W(1)-W(2) pair. Some diffraction data indicate that the W vibrations are nearly isotropic[7] while Fig. 7(a) of Ref. 25 shows prolate thermal ellipses oriented along $\langle 111 \rangle$. EXAFS analysis is not very sensitive to the motion perpendicular to a $\langle 111 \rangle$ axis and cannot distinguish between these two possibilities.

There is, however, a disagreement regarding the motions of the O3 atom. The thermal ellipses obtained from neutron-diffraction data at 293 K suggest that the O(3) atom [the unconstrained O atom for W(2)] has a motion mainly perpendicular to the $\langle 111 \rangle$ axis[2,25] which is in disagreement with our above analysis. [For the O(4) atom, the thermal ellipse is quite large in both directions, so the possibility of a large vibration along the $\langle 111 \rangle$ axis is not inconsistent]. Although the thermal ellipse at 293 K is shown with the largest axis perpendicular to the $\langle 111 \rangle$ axis (oblate spheroid), the complete data set (supplementary data for Ref. 25) indicates that the thermal ellipse is a prolate spheroid with the long axis along the $\langle 111 \rangle$ axis for data at six out of eight temperatures. In a second paper with much poorer S/N but many more temperatures,[7] Evans *et al.* also obtain an oblate thermal ellipsoid for O3. However, the oblate spheroid they obtain for O3 has a serious problem; for motion along the $\langle 111 \rangle$ axis, the W2 vibration is much larger than that for O3, i.e., the W is vibrating relative to the O3 atom along $\langle 111 \rangle$. This is inconsistent with the large mass difference between W and O. On the other hand, the prolate spheroid has the expected result that the O motion along $\langle 111 \rangle$ is larger than that of W.

E. Tent-pole model

Based on the analysis above, we develop a simplified local vibrational mode for the low-frequency optical phonons. We propose that this model contains the essential physics that leads to NTE in ZrW$_2$O$_8$. Figure 14 shows a simplified cutaway structure, which consists of three WO$_4$ tetrahedra (two W$_1$ and one W$_2$) and all their nearest ZrO$_6$ octahedra plus two isolated ZrO$_6$ octahedra which are aligned along one of the four $\langle 111 \rangle$ axes. Each tetrahedron is surrounded by three ZrO$_6$ octahedra which form a plane perpendicular to the $\langle 111 \rangle$ axis of the crystal. The unshared corner of each tetrahedron points along a $\langle 111 \rangle$ axis. As a WO$_4$ tetrahedron moves along this $\langle 111 \rangle$ axis, the three nearest ZrO$_6$ octahedra will move together due to the stiffness of the W-O-Zr linkage and rotate slightly because of the corner connections to other units. Note that for this motion the WO$_4$ is unconstrained along the $\langle 111 \rangle$ direction and can move into unoccupied space. Also, there are no atoms between any pair of ZrO$_6$ octahedra to constrain their translational motion.
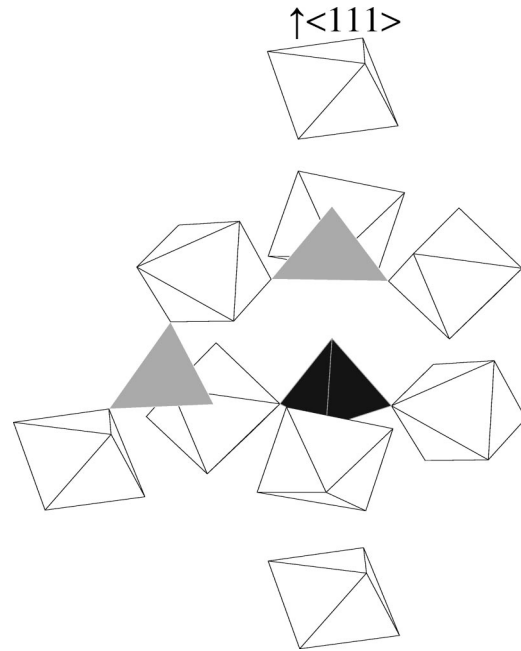

FIG. 14. A cutaway section of the unit cell after removing many of the polyhedra; it shows the remaining W(1)O$_4$ (gray) and W(2)O$_4$ (black) tetrahedra and ZrO$_6$ octahedra. From this point of view, each tetrahedron is connected to three ZrO$_6$ octahedra which form a plane perpendicular to a $\langle 111 \rangle$ axis. Each tetrahedron vibrates vertically to this plane.

We now consider the motions of the three nearest Zr atoms while a W atom vibrates along a $\langle 111 \rangle$ axis. In Fig. 15, we present a "rigid-tentpole model" to show how the Zr-Zr distance changes with the W motion. The oxygen atoms are omitted for simplicity, the W-Zr linkages are assumed here to be rigid (the tent poles), and the W is initially in the plane of the Zr. When W moves away from the plane of the Zr atoms, either up (as in a tent) or down, the Zr atoms move closer together because of the stiff W-Zr link. Since such motions occur on all four $\langle 111 \rangle$ axes, we expect an isotropic contrac-
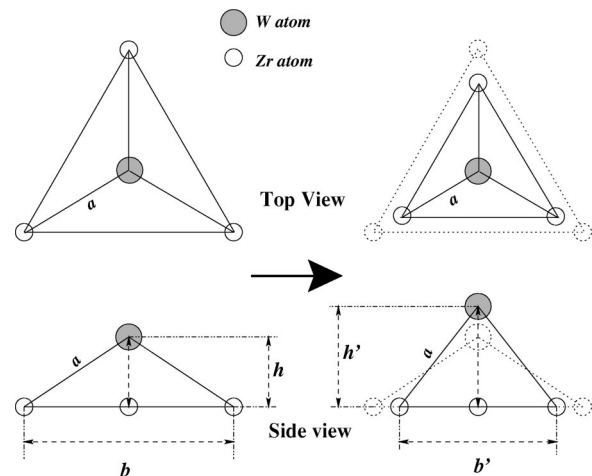

FIG. 15. A plot to show the correlated motions between W and Zr atoms. The O atoms in between are neglected in order to make it clearer.

tion which agrees with diffraction results. In the real lattice, the tetrahedra and octahedra must also tilt/rotate and the Zr-O bond stretch slightly to maintain the lattice structure. The motions are similar in some respects to the more complicated model presented in Ref. 25. There the focus was on rotations of the polyhedra, while vibrations that included translations of the polyhedra were not considered; the main modes in their model correspond to a transverse vibration of some of the O atoms. In our model the low-energy mode involves large motions of the heavy W and Zr atoms.

F. Soft-mode frustration

As illustrated in Fig. 1, the crystal structure of ZrW_2O_8 is open, and measurements of both the phonon density of states and specific heat show that there are very low-energy optical modes which are associated with the negative thermal expansion in this material. These low-energy modes are therefore candidates for a possible soft-mode phase transition in ZrW_2O_8. In many other systems a low-frequency optical-phonon mode can correspond to a particular local distortion of the lattice. If the frequency of this soft mode decreases (referred to as a mode softening) and goes to zero, the distortion then becomes static and leads to a symmetry-lowering phase transition. In fact, another high-temperature NTE material, ZrV_2O_7, a close structural relative of ZrW_2O_8, shows a symmetry-lowering phase transition as its isotropic NTE vanishes below 373 K.[8] However, ZrW_2O_8 displays an isotropic NTE and remains a cubic lattice to very low temperature. Thus the answer to the question of why ZrW_2O_8 doesn't undergo a soft-mode phase transition is important for understanding NTE in this system.

An important aspect of this problem concerns the degeneracy of the vibration modes that we have identified. The low-temperature specific heat indicates that there are four low-frequency modes per unit cell that contribute; fits to the specific-heat data show that there are two Einstein frequencies with amplitudes in the ratio of roughly 1:3.[10] This amplitude ratio does not appear in the phonon density of states[11]—the two lowest peaks overlap and appear to have similar peak heights. However, one needs the width of the dispersion for each mode before comparing with the delta-function Einstein modes used in the specific-heat analysis.

The EXAFS results indirectly support the 1:3 ratio of the mode intensities. There are four possible local vibrations of W_1-W_2 along the four equivalent $\langle 111 \rangle$ axes per unit cell. These modes appear to be degenerate because of the equivalency of the $\langle 111 \rangle$ axes; however, a fourfold degeneracy is not compatible with cubic symmetry. Using group theory and the 12 symmetry operations for this space group ($P2_13$) these four modes break up into a singlet and a triplet and hence would have amplitudes in the ratio of 1:3. Thus the modes we have identified are also consistent with the specific-heat data. With the singlet as the lowest mode[10] there is no degeneracy that can be lifted by a symmetry-lowering distortion at low temperatures and hence no reason for a displacive transition to occur.

A detailed examination of the lattice structure also suggests that the WO_4 vibrations along different $\langle 111 \rangle$ axes are
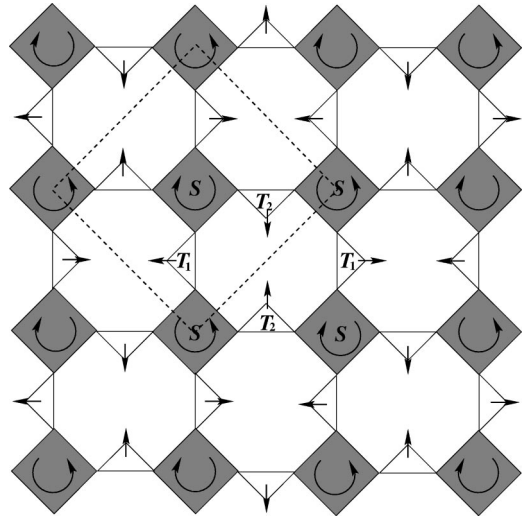

FIG. 16. A two-dimensional system with a similar structure to the ZrW_2O_8. Both squares and triangles are distortion-free in this system. All four corners of each square are shared with different triangles, while each triangle only shares two of its three corners with squares and leave one corner unconstrained. A further constraint in this system is that the triangles can translate but not rotate. Under uniaxial compression, the squares rotate as shown and the lattice contracts in both directions. A similar model was discussed by Simon and Varma (Ref. 26).

coupled which leads to the splitting of the singlet and triplet discussed above. As a WO_4 tetrahedron translates, its three nearest ZrO_6 octahedra rotate slightly and move together (or apart) as described in the discussion of the tentpole model. These motions in turn drive the motions of other WO_4 tetrahedra through the relatively rigid W-O-Zr linkage. See Ref. 27 for further details. This coupling of W motions along different $\langle 111 \rangle$ axes leads to the prediction that if the correlated motions occur at $k=0$, the application of a uniaxial pressure (for example, along the x axis) to the ZrW_2O_8 unit cell will lead to a contraction along the other two axes as well. This effect is called a "negative Poisson ratio" (NPR). Usually when uniaxial pressure is applied to a material (with a positive Poisson ratio) the material will expand along the other axes in order to keep its original volume. An example of a system with a NPR is the "Hoberman™ sphere": the whole sphere will contract or expand symmetrically when a uniaxial force is applied upon it.

Figure 16 shows a simplified two-dimensional model of such a system with NPR: it consists of connected squares and triangles. All units are rigid and the triangles are constrained to not rotate. There are two sets of triangles in this system: triangles with two constrained corners along the y axis (vertically) are called T_1, and those with two constrained corners along the x axis (horizontally) are called T_2. When uniaxial pressure is applied along the y axis, the squares S will rotate and the T_1 triangles will translate along the x axis as the system contracts along this axis. In addition, the rotations of each square also drive translations of T_2 along the y axis, leading to a net contraction along the x axis as well. In the ZrW_2O_8 system, due to the effect of further-neighbor interactions, the NPR might only occur within the

nanometer scale. Further experiments will be carried out to see if the ZrW_2O_8 bulk sample also displays a negative Poisson ratio.

V. CONCLUSION

The XAFS results clearly show that the WO_4 tetrahedra are rigid, while the ZrO_6 octahedra are stiff but not rigid as temperature increases from ~ 0 to 315 K. The small temperature dependence of σ^2 for the W-Zr peak indicates that the W-O-Zr linkage is quite stiff over the same temperature range, which therefore suggests the existence of an even larger quasirigid unit involving a WO_4 tetrahedron and its three nearest ZrO_6 octahedra. The small magnitude and weak temperature dependence of σ^2_{W-Zr} shows that the motions of the W, O, and Zr atoms are correlated and therefore cannot be considered independently. Consequently the simple RUM models are not appropriate—at least at 300 K. The stiffness of the W-O-Zr linkage also indicates that the transverse vibrations of the O atom in the middle of the W-O-Zr linkage cannot be the primary origin of the negative thermal expansion in ZrW_2O_8.

The much larger temperature dependence of σ^2 for the nearest W_1-W_2 and Zr-Zr pairs indicates that vibrations of these atom pairs produce the low-energy optical modes in this system that are considered to be the origin of NTE in ZrW_2O_8. The cusp around 100 K on the σ^2 vs T plot for the W-W and Zr-Zr atom pairs indicates a mode hardening just above 100 K while the temperature dependence of σ^2 yields an Einstein temperature of ~ 45 K at low temperatures. Both results agree with the measurements of the phonon density of states and therefore provide further confirmation that the W-W and Zr-Zr vibrations produce the low-frequency optical modes. A simplified rigid-tentpole model based on the XAFS results suggests the form of the local vibrational mode. The rigidity of the WO_4 units implies that the WO_4 tetrahedra must translate along the $\langle 111 \rangle$ directions.

The lack of a soft-mode phase transition in this system is due to a coupling of the vibrations of WO_4 tetrahedra along all four $\langle 111 \rangle$ axes which leads to the formation of singlet and triplet states. Each of these eigenmodes is a linear combination of vibrations along each of the $\langle 111 \rangle$ axes and consequently each would produce an isotropic thermal contraction. The overall contraction is constrained by the lattice structure. These modes should cover the entire range in k space. If this is true for the $k = 0$ mode then this system may exhibit a negative Poisson ratio. It remains to be tested whether or not bulk ZrW_2O_8 shows a NPR because of the further-neighbor interactions.

[1] C. Martinek and F.A. Hummel, J. Am. Ceram. Soc. **51**, 227 (1968).

[2] T.A. Mary, J.S.O. Evans, T. Vogt, and A.W. Sleight, Science **272**, 90 (1996).

[3] W.I.F. David, J.S.O. Evans, and A.W. Sleight, Europhys. Lett. **46**, 661 (1999).

[4] M. Blackman, Philos. Mag. **9**, 831 (1958).

[5] R. Roy, D.K. Agrawal, and H.A. McKinstry, Annu. Rev. Mater. Sci. **19**, 59 (1989).

[6] A.W. Sleight, Endeavour **19**, 64 (1995).

[7] J.S.O. Evans, W.I.F. David, and A.W. Sleight, Acta Crystallogr., Sect. B: Struct. Sci. **B55**, 333 (1999).

[8] V. Korthuis, N. Khosrovani, A.W. Sleight, N. Roberts, R. Dupree, and W.W. Warren, Chem. Mater. **7**, 412 (1995).

[9] A.K.A. Pryde, K.D. Hammonds, M.T. Dove, and V.H. Etal, J. Phys.: Condens. Matter **8**, 10 973 (1996).

[10] A.P. Ramirez and G.R. Kowach, Phys. Rev. Lett. **80**, 4903 (1998).

[11] G. Ernst, C. Broholm, G.R. Kowach, and A.P. Ramirez, Nature (London) **396**, 147 (1998).

[12] R. Mittal and S.L. Chaplot, Phys. Rev. B **60**, 7234 (1999).

[13] R. Mittal and S.L. Chaplot, Solid State Commun. **115**, 319 (2000).

[14] R. Mittal, S.L. Chaplot, H. Schober, and T.A. Mary, Phys. Rev. Lett. **86**, 4692 (2001).

[15] G.G. Li, F. Bridges, and C.H. Booth, Phys. Rev. B **52**, 6332 (1995).

[16] F. Bridges, C.H. Booth, and G.G. Li, Physica B **208&209**, 121 (1995).

[17] J.J. Rehr, C.H. Booth, F. Bridges, and S.I. Zabinsky, Phys. Rev. B **49**, 12 347 (1994).

[18] B. K. Teo, *EXAFS: Basic Principles and Data Analysis* (Springer-Verlag, New York, 1986).

[19] *X-Ray Absorption Principles*, *Applications Techniques of EXAFS SEXAFS XANES*, edited by D. Koningsberger and R. Prins (Wiley, New York, 1988).

[20] S.I. Zabinsky, J.J. Rehr, A. Ankudinov, R.C. Albers, and M.J. Eller, Phys. Rev. B **52**, 2995 (1995).

[21] J.D. Jorgensen, Z. Hu, S. Teslic, D.N. Argyriou, S. Short, J.S.O. Evans, and A.W. Sleight, Phys. Rev. B **59**, 215 (1999).

[22] E.A. Stern, Phys. Rev. B **48**, 9825 (1993).

[23] The amplitude, A, of a peak in r-space XAFS data can be written as $A_i \propto D_i / r_i^2$, where r_i is the distance from center atom to backscatter atoms in the ith shell, and D_i is the degeneracy of this scattering path. For the nearest W-O bonds in ZrW_2O_8, D_i is 4 and r_i is ~ 1.75 Å, while for the longer W-O bond, D_i and r_i are 0.5 [only W(1) has this bond] and 2.4 Å, respectively. Therefore the amplitude of this longer W-O peak at 2.4 Å is about 1/15 of that for the shortest W-O peak in W L_{III}-edge r-space data for ZrW_2O_8.

[24] F. Bridges, G. Brown, D. Cao, and M. Anderson, J. Synchrotron Radiat. **8**, 366 (2001).

[25] J.S.O. Evans, T.A. Mary, T. Vogt, M.A. Subramanian, and A.W. Sleight, Chem. Mater. **8**, 2809 (1996).

[26] M.E. Simon and C.M. Varma, Phys. Rev. Lett. **86**, 1781 (2001).

[27] D. Cao, F. Bridges, G.R. Kowach, and A.P. Ramirez, Phys. Rev. Lett. **89**, 215902 (2002).